PHOTONICS Research

Third-order nonlinear optical susceptibility of crystalline oxide yttria-stabilized zirconia

Guillaume Marcaud,[1,*,†] Samuel Serna,[1,2,3,†] Karamanis Panaghiotis,[4,†] Carlos Alonso-Ramos,[1] Xavier Le Roux,[1] Mathias Berciano,[1] Thomas Maroutian,[1] Guillaume Agnus,[1] Pascal Aubert,[1] Arnaud Jollivet,[1] Alicia Ruiz-Caridad,[1] Ludovic Largeau,[1] Nathalie Isac,[1] Eric Cassan,[1] Sylvia Matzen,[1] Nicolas Dubreuil,[5,6] Michel Rérat,[4] Philippe Lecoeur,[1] and Laurent Vivien[1,7]

[1]Centre de Nanosciences et Nanotechnologies (C2N), Université-Paris-Sud, CNRS UMR 9001, Université Paris-Saclay, Orsay 91405, France
[2]Current address: Department of Materials Science and Engineering, Massachusetts Institute of Technology, Cambridge, Massachusetts 02139, USA
[3]Department of Physics, Bridgewater State University, Bridgewater, Massachusetts 02325, USA
[4]Institut des Sciences Analytiques et de Physico-Chimie pour l'Environnement et les Matériaux, CNRS, Université de Pau et des Pays de l'Adour, 64053 Pau Cedex, France
[5]Laboratoire Charles Fabry, Institut d'Optique Graduate School, CNRS, Université Paris-Saclay, 91127 Palaiseau Cedex, France
[6]Current address: LP2N, Institut d'Optique Graduate School, CNRS, Univ. Bordeaux, 33400 Talence, France
[7]e-mail: laurent.vivien@c2n.upsaclay.fr
*Corresponding author: guillaume.marcaud@c2n.upsaclay.fr

Received 30 August 2019; revised 5 November 2019; accepted 9 November 2019; posted 12 November 2019 (Doc. ID 375869); published 13 January 2020

Nonlinear all-optical technology is an ultimate route for the next-generation ultrafast signal processing of optical communication systems. New nonlinear functionalities need to be implemented in photonics, and complex oxides are considered as promising candidates due to their wide panel of attributes. In this context, yttria-stabilized zirconia (YSZ) stands out, thanks to its ability to be epitaxially grown on silicon, adapting the lattice for the crystalline oxide family of materials. We report, for the first time to the best of our knowledge, a detailed theoretical and experimental study about the third-order nonlinear susceptibility in crystalline YSZ. Via self-phase modulation-induced broadening and considering the in-plane orientation of YSZ, we experimentally obtained an effective Kerr coefficient of $\widehat{n}_2^{\mathrm{YSZ}} = 4.0 \pm 2 \times 10^{-19}\ \mathrm{m^2 \cdot W^{-1}}$ in an 8% (mole fraction) YSZ waveguide. In agreement with the theoretically predicted $\widehat{n}_2^{\mathrm{YSZ}} = 1.3 \times 10^{-19}\ \mathrm{m^2 \cdot W^{-1}}$, the third-order nonlinear coefficient of YSZ is comparable with the one of silicon nitride, which is already being used in nonlinear optics. These promising results are a new step toward the implementation of functional oxides for nonlinear optical applications.

https://doi.org/10.1364/PRJ.8.000110

1. INTRODUCTION

Integrated nonlinear photonics has reached the point of meeting demands of on-chip optical processing and transmission, owing to the CMOS compatibility. Silicon in particular presents the ability of strong optical confinement. Nevertheless, some properties of silicon are not adequate for integrated photonics. Notably, it presents a large two-photon absorption (TPA) in the near-infrared, while it is accompanied by a large third-order nonlinear susceptibility. This condition limits the use of silicon for devices exploiting Raman lasing [1], Brillouin amplification [2], or parametric amplification [3]. In this context, the quest for other materials, as compatible as possible with silicon foundries, started several years ago.

In these new plethora of options, promising results have been obtained in silicon nitride [4], amorphous silicon [5], or arsenic-free chalcogenides [6], thus exploiting third-order nonlinearities. More broadly, strongly correlated materials like crystalline oxides have emerged as a promising family for their large variety of properties from ferroelectricity, optical nonlinearities to ferromagnetism, or phase transition. The combination of their tunable properties leads to the development of innovative devices with manifold functionalities in many fields

such as solar cells [7], sensors [8], electronics [9], or optics [10], to name a few. However, optical nonlinearities of crystalline oxides are still unknown for the most part.

Among the crystalline oxides, yttria-stabilized zirconia (YSZ) is known for its role as a buffer layer for the integration of $LiNbO_3$, $PbTiO_3$, $Pb(Zr, Ti)O_3$, and $YBa_2Cu_3O_7$ thin films on silicon [11–14] and as a solid electrolyte due to its high ionic conductivity [15]. In addition, YSZ exhibits extraordinary thermal, mechanical, and chemical stability [16–18] as well as high refractive index about 2.15 in the telecom wavelength range and a wide transparency window from UV to mid-IR [16,19–21].

Thanks to the development of growth technique, YSZ has recently demonstrated its potential as a new material for low-loss optical waveguides and as a flexible substrate for infrared nano-optics [22,23]. However, nonlinear optical properties of YSZ have never been investigated.

We present in this work a theoretical study of the third-order nonlinearities of YSZ and its experimental characterization. First-principle calculations were performed to understand the concentration and doping distribution dependence of the third-order nonlinearities in YSZ. Then, we grew high-quality YSZ thin films and fabricated a low-loss waveguide with an optimized material composition. Finally, thanks to a sensitive technique described in detail in Ref. [24], we have characterized the optical nonlinearities of YSZ. The experimental results presented in this paper agree with the calculations and provide a strong first step toward the promising integration of crystalline oxide in a silicon photonics platform.

2. FIRST-PRINCIPLE CALCULATIONS

Assuming that the optical nonlinearities of YSZ should stem from the intrinsic nonlinear optical (NLO) properties of the doping substrate, namely, the cubic phase of ZrO_2 (c-ZrO_2), we proceeded as follows. First, we focused on the static nonlinear optical properties of pure c-ZrO_2 aiming at a reliable estimation of the order of magnitude of its third-order NLO responses in idealized conditions to be used as a guide for our qualitative conclusions. Because little is known about the true local atomistic structure of YSZ, to circumvent the challenging task [25,26] of determining the most stable local crystal structure of each system considered, the second step comprised computations addressing the importance of the vacancy/dopant distribution on the third-order susceptibilities. For this task, we chose two doping concentrations of 3.2% and 33% (mole fraction, hereinafter the same unless specified otherwise) in Y_2O_3 representing the dilute limit and a relatively high doping concentration, respectively. Finally, the third and last step of the current theoretical investigation involved simulations on YSZ of increasing concentrations in Y_2O_3.

In this work, the relative dielectric ϵ matrix and nonlinear $\chi^{(n)}$ susceptibility tensors were obtained from the electronic part [27] of the polarizability (α^e) and the first (β^e) and second (γ^e) order hyperpolarizabilities of the unit cell as

$$\epsilon_{ij} = \delta_{ij} + 4\pi\alpha^e_{ij}/V, \quad (1)$$

$$\chi^{(2)}_{ijk} = 2\pi\beta^e_{ijj}/V, \quad (2)$$

$$\chi^{(3)}_{ijkl} = 2\pi\gamma^e_{ijkl}/(3V), \quad (3)$$

where V is the volume of the unit cell and δ_{ij} represents the Kronecker delta. Note that an ideal cubic structure features one independent ϵ_{ii} and two $\chi^{(3)}_{iiii}$ and $\chi^{(3)}_{iijj}$ components, respectively, while the total second-order nonlinear optical response $\chi^{(2)}$ vanishes.

Bearing in mind that the computation of third-order susceptibilities of molecules, polymers, and solids greatly depends on the quantum chemical method applied [28–30], we computed the third-order optical nonlinearities of pure and doped bulk systems using three DFT functionals within the generalized gradient approximation (GGA). These are the pure Perdew, Burke, and Ernzerhof (PBE) [31] exchange-correlation functional; its hybrid counterpart PBE0 [32]; and the Becke, three-parameter, Lee–Yang–Parr exchange-correlation functional (B3LYP) [33]. The first two functionals, namely, PBE and PBE0, have been used in previous studies [25,34], involving the structural and electronic properties of YSZ, while the popular B3LYP was chosen in order to check the robustness of the results. All periodic calculations have been performed at the static limit with a developer's version of CRYSTAL17 software [35], which allows analytic computations of nonlinear optical (NLO) properties of infinite periodic systems. We also performed benchmark computations focusing on the molecular second dipole hyperpolarizabilities of $(ZrO_2)_n$ nanoclusters at CCSD(T) (coupled cluster including single, double, and triple excitations) and MP2 (second-order Möller–Plesset perturbation theory) levels using the GAUSSIAN09 [36] suit of programs.

Third-order nonlinearities of c-ZrO_2. The results of the respective computations are summarized in Table 1, where we present lattice constants, bandgaps, the electronic contribution to the dielectric constant, and the two independent $\chi^{(3)}$ tensorial components of c-ZrO_2. For the sake of brevity, a more detailed discussion of these outcomes is given in Appendix A. Here, we will only mention that the observed method behavior, characterized by notable oscillations in the computed bulk nonlinearities, is in line with that of previous studies [28–30] performed on finite atomic semiconductor nanoclusters. Interestingly, the current computations reveal that the known pathology of pure DFT functionals effect also concerns the computed dielectric constants for which experimental results are available (see values listed in Table 1). Nonetheless, and in spite of the obvious deviations, the obtained results allow us to make the following deductions. First, for c-ZrO_2,

Table 1. Cell Parameter a (Å), Bandgap E_g (eV), Electronic Contribution of the Dielectric Constant $\epsilon = \epsilon_{ii}$, and Third-Order Susceptibility Components $\chi^{(3)}_{iiii,iijj}$ (10^{-21} m$^2 \cdot$ V^{-2}) of c-ZrO_2 Computed with the PBE, PBE0, and B3LYP Functionals

	PBE	PBE0	B3LYP	Exp
a	5.127	5.090	5.132	5.09 [37], 5.135 [38]
E_g	3.1	5.4	4.9	4.5 [39], 4.6 [40]
ϵ	5.49	4.43	4.57	4.46[a]
$\chi^{(3)}_{iiii}$	7.60	1.53	1.91	
$\chi^{(3)}_{iijj}$	3.80	1.25	1.52	

[a]Calculated from Ref. [41] at $\lambda = 1500$ nm.

characterized by a rather wide bandgap, all three DFT methods yielded third-order susceptibilities of the same order of magnitude varying between 7.6 and 1.53×10^{-21} m$^2 \cdot$ V^{-2} for the tensorial component $\chi^{(3)}_{iiii}$ and between 3.8 and 1.25×10^{-21} m$^2 \cdot$ V^{-2} for $\chi^{(3)}_{iijj}$. Second, considering that $\chi^{(3)}$ can be written as an infinite sum of terms [42] inversely proportional to the cubic power of transition energies, the obtained outcomes at PBE0, B3LYP, and PBE levels indicate that, as we approach the experimental bandgap value from above/below, one should expect larger/smaller theoretical values for both $\chi^{(3)}_{iiii}$ and $\chi^{(3)}_{iijj}$. Third, taking into account that pure DFT functionals, as PBE, systematically overshoot the (non)linear optical properties of molecular systems [43], we expect that the upper limit of the theoretically determined components $\chi^{(3)}_{iiii}/\chi^{(3)}_{iijj}$ of c-ZrO_2 should be considerably lower than 7.6 and 3.8×10^{-21} m$^2 \cdot$ V^{-2}, respectively. The latter conclusions are supported by a brief DFT functional performance assessment, on the computation of the molecular second dipole hyperpolarizabilities of three $(ZrO_2)_n$ nanoclusters [44], namely, Zr_4O_8, Zr_8O_{16}, and $Zr_{15}O_{30}$ with respect to CCSD(T) and MP2 *ab-initio* post Hartree–Fock methods. The respective computations, presented in Appendix A, also exposed the pivotal importance of electron correlation effects on the third-order optical nonlinearities of $(ZrO_2)_n$ species.

Doping and vacancy/dopant distribution effects on the optical nonlinearities of YSZ. To conduct the respective structure property investigation, we considered doped bulk YSZ systems of two concentrations in Y_2O_3, namely, 33% and 3.2%. For the highest dopant concentration, two different compensated unit cells were built upon the face-centered cubic (fcc) $Fm\bar{3}m$ cell of zirconium dioxide (volume = 131.9 Å^3, $E_g = 5.37$ eV) by removing one O atom from its tetrahedral site, thus creating an oxygen vacancy. Then, two out of the four nearest-neighbor (NN) Zr atoms of the corresponding vacancy were substituted by an equal number of Y atoms, delivering two nonequivalent NN crystal structures of Y_2O_3, $2ZrO_2$. The equilibrium nuclear geometry of each unit cell and their optical nonlinearities were optimized with the PBE0 functional. In the case of 3.2% in Y_2O_3, we considered the 10 most stable nonequivalent configurations reported by Parkes *et al.* [25], the crystal structures of which were built upon a doped $2 \times 2 \times 2$ super cell of c-ZrO_2, optimized with the PBE functional.

The computed electronic and optical properties of the two crystal configurations of YSZ 33% in Y_2O_3 are given in Table 2. Both crystal structures are characterized by equal bandgap values and reduced third-order nonlinearities to those obtained for pure c-ZrO_2 (see Table 1). Judging from the relative strengths of each component along the $x \equiv y$ and z axis, we see that, although the creation of an O vacancy and the replacement of two Zr atoms with Y reduces the cubic symmetry of the host, the third-order NLO responses remain quasi-isotropic in character because $\chi^{(3)}_{xxxx,xxyy} \approx \chi^{(3)}_{zzzz,xxzz}$. Hence, even for a relatively high yttria concentration, YSZ inherits most of the isotropic nonlinear optical nature of c-ZrO_2. A similar property trend is obtained for all configurations of Y_2O_3 3.2% considered here.

Table 2. Unit Cell Volume V (Å^3), Bandgap E_g (eV), Electronic Contribution to the Dielectric $\epsilon_{xx} = \epsilon_{yy}$ and ϵ_{zz} Components, and Kerr (IDRI) Effect Third-Order Susceptibility $\chi^{(3)}_{xxxx} = \chi^{(3)}_{yyyy}, \chi^{(3)}_{zzzz}$, and $\chi^{(3)}_{xxyy}, \chi^{(3)}_{xxzz} = \chi^{(3)}_{yyzz}$ Components (10^{-21} m$^2 \cdot$ V^{-2}) of Two Nonequivalent Local Crystal Structures of YSZ 33% in Y_2O_3 (see Fig. 2)[a]

	YSZ-A	YSZ-B
V	132	138
E_g	5.6	5.6
ϵ_{xx}	3.7	3.5
ϵ_{zz}	3.5	3.3
$\chi^{(3)}_{xxxx}$	0.93	0.69
$\chi^{(3)}_{zzzz}$	0.86	0.89
$\chi^{(3)}_{xxyy}$	0.70	0.65
$\chi^{(3)}_{xxzz}$	0.62	0.62

[a]All properties have been computed with the PBE0 functional.

As shown in Fig. 1, the influence of the vacancy/dopant distribution on the properties of interest is practically negligible. Furthermore, for both concentrations, we also computed the corresponding second-order susceptibilities. In all cases, the computed second-harmonic generation $\chi^{(2)}(-2\omega; \omega, \omega)$ for $\omega = 0.8$ eV (corresponding to the wavelength $\lambda = 1550$ nm) has been proven considerably small. Indeed, the largest absolute xyz component value of $\chi^{(2)}$ for the most stable YSZ 33% structure is lower than 0.014 pm $\cdot$ V^{-1}.

In comparison with the c-ZrO_2, the weak bandgap opening of about 0.2 eV observed in YSZ 33% in Y_2O_3 should not justify the observed lowering in the third-order susceptibilities. Hence, bearing in mind that the third-order nonlinearities of charge transfer insulators [45] should depend on the amount of electron and hole states lying near the gap, the observed effect could be primarily attributed to the doping-induced reduction of the density of low-lying hole states in the conduction band. This is well illustrated by the projected density of states (PDOS) of YSZ 33% [see Fig. 2(b)], where the DOS projected on Zr atoms (3p in character), located at the bottom of the conduction band, drastically decreases after the replacement of two Zr atoms with an equal number of Y. On the other hand, the creation of an O vacancy does not introduce important changes in the valence band (O-2p-in-character) of c-ZrO_2. These are two enlightening trends, suggesting that the third-order nonlinear optical responses of doped c-ZrO_2 could be further improved with doping agents that are able to deliver a significant increase of low-lying hole states.

Concentration dependence. Thus far, the obtained computational data has revealed that the cubic phase of pure c-ZrO_2 is characterized by third-order nonlinearities lying above the limit of 1×10^{-21} m$^2 \cdot$ V^{-2}. Also, computations on two different concentrations of YSZ (33% and 3.2% in Y_2O_3) provided solid proof that Y-doping delivers a notable lowering of the respective nonlinear optical responses whatever the vacancy/dopant distribution in the crystalline phase. In this section, we briefly focus on variation of the $\chi^{(3)}_{iiii}$ and $\chi^{(3)}_{iijj}$ components of YSZ as a function of the Y_2O_3 concentration. For this task, we considered three concentrations of YSZ, namely, 7%, 14%, and 33% (mole fractions). All unit cells of the doped

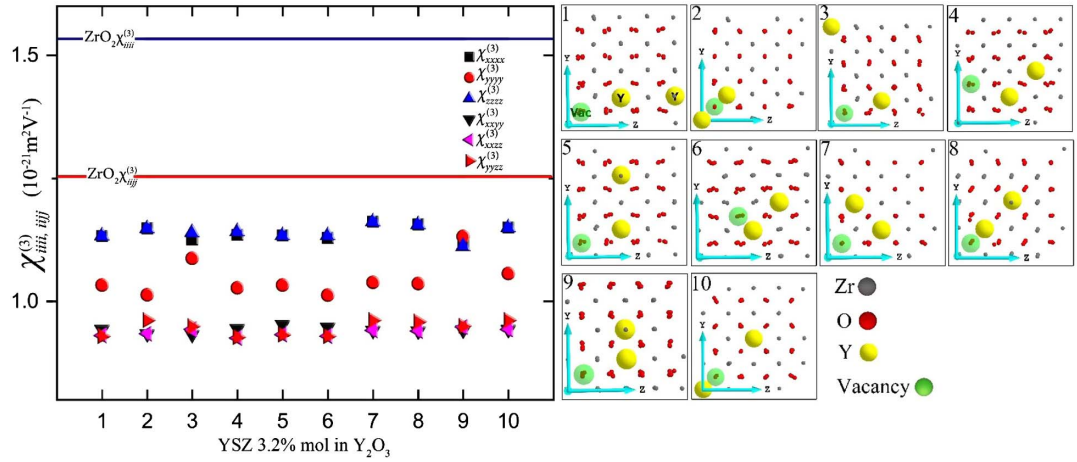

Fig. 1. Variation of the third-order susceptibility tensorial components ($\chi_{iiii,iijj}$) of YSZ 3.2% in Y_2O_3 as a function of the relative position between Y dopants (yellow spheres) and O vacancies (green spheres). The unit cells [25] of each configuration considered, representing symmetry in equivalent vacancy/dopant distributions, are schematically given at the right. Solid lines represent the corresponding susceptibility components of c-ZrO_2. All values have been computed at the PBE0 level of theory.

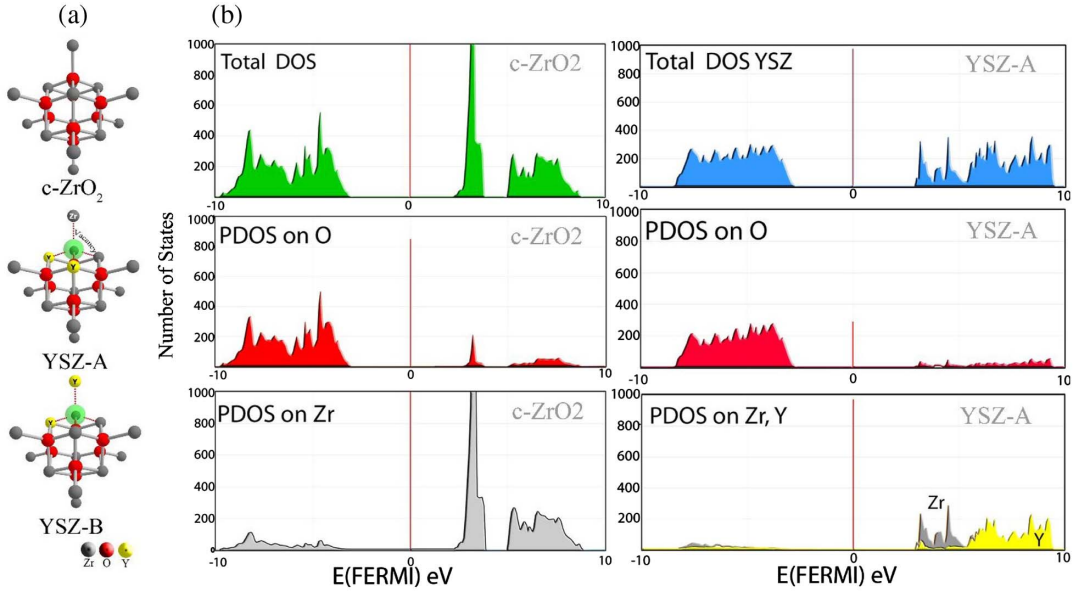

Fig. 2. (a) Symmetry nonequivalent local crystal structures of YSZ 33% in Y_2O_3. Zirconium, oxygen, and yttrium atoms are in gray, red, and yellow, respectively, and the vacancy is in green. See Data File 1 and Data File 2 for the unit-cell fractional coordinates of YSZ-A and YSZ-B, respectively. (b) Total and projected density of states of c-ZrO_2 and YSZ-A.

bulk systems were built upon compensated super-cells of c-ZrO_2 of appropriate sizes in order to obtain each of the desired concentration in Y_2O_3. Unit-cell fractional coordinates of the four YSZ systems considered, 7%, 14%, 33%-A, and 33%-B, are reported in the supplementary material.

In every local crystal structure, the NN doping method has been adopted without performing further structural investigations for the determination of the most stable atomistic crystal structure. The obtained property evolution, depicted in Fig. 3, clearly demonstrates that YSZ third-order susceptibilities increase in a rather monotonic fashion while decreasing the concentration in Y_2O_3. Therefore, the optimal YSZ bulk system for photonic applications, built upon c-ZrO_2, should feature the lowest concentration in Y_2O_3 that ensures the stability of the cubic phase of the respective crystal at room temperature.

3. EXPERIMENTAL CHARACTERIZATION

The intensity-dependent refractive index (IDRI) Kerr property of YSZ has been characterized via the Kerr-induced self-phase modulation (SPM), in a YSZ-based waveguide directly fabricated in the YSZ 8% thin film.

The growth of high-quality YSZ thin film is performed with an optimized pulsed-laser deposition process on sapphire

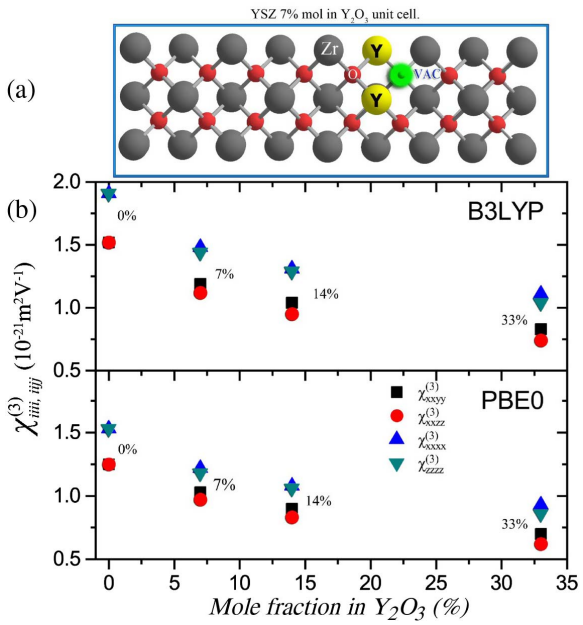

Fig. 3. (a) Unit cell of YSZ 7% considered in this study. (b) Evolution of $\chi^{(3)}_{iiii}$ and $\chi^{(3)}_{iijj}$ of YSZ as a function of the concentration in Y_2O_3 computed with the B3LYP and PBE0 functionals and the smallest ECP basis set used in this work. All local crystal structures have been optimized at the PBE0 level of theory. See Data File 3 and Data File 4 for the unit-cell fractional coordinates of YSZ 7% and YSZ 14%, respectively.

(0001), described in detail in Ref. [22]. We demonstrated that the [001] growth direction of YSZ can be largely promoted with up to six in-plane grain orientations separated by 15 deg. The characterization by X-ray diffraction (XRD) of the $H = 300$ nm thick film used in this work is presented in Figs. 4(d) and 4(e). The $2\theta - \omega$ XRD scan mode confirms the only [001] YSZ growth direction on sapphire, whereas the mosaicity is estimated via the full width at half maximum (FWHM = 0.03°) of the (002) YSZ peak of the ω scan.

YSZ waveguides are designed to confine and propagate a single quasi-TE optical mode in the telecom wavelength range. After an optimized fabrication process based on electron-beam lithography and ion-beam etching techniques, waveguide dimensions are measured by atomic-force microscopy (AFM), as represented with the topographic profile, as shown in Fig. 4(b). The etching depth is $D = 80$ nm, and waveguide width W is about 760 nm. Propagation losses $\alpha = 3.2$ dB $\cdot$ cm^{-1} at $\lambda = 1550$ nm are measured for the quasi-TE mode thanks to the comparison of transmission levels from different waveguides on the sample, long from $L = 0.8$ mm to $L = 5.8$ mm. These loss measurements are performed with grating couplers, located at each waveguide extremity and fabricated with the same process in the YSZ thin film.

As a nonlinear phenomenon, the Kerr effect characterization in YSZ waveguides strongly depends on the light–matter interaction and thus on the injected optical power. In order to improve the light injection, we have therefore considered the butt coupling configuration and the longest waveguide available on the chip with a length of $L = 5.8$ mm.

The experimental setup used for the characterization of the YSZ samples is described in Ref. [46]. It consists of a mode-locked erbium-doped fiber laser that delivers 150 fs duration pulses with a repetition rate of $F = 50$ MHz for a wavelength of $\lambda = 1580$ nm. After passing through a polarization beam splitter that guarantees the polarization state to excite the fundamental TE mode, the pulses are shaped through a grating-based stretcher that fixes the pulse spectrum following a quasi-rectangular shape of variable widths and introduces an

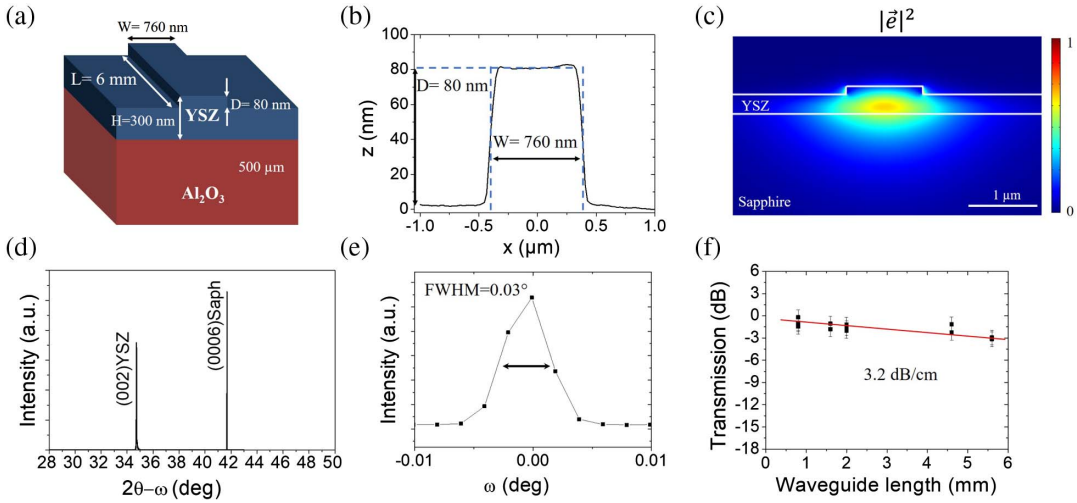

Fig. 4. (a) Schematic view of a YSZ-based rib waveguide, designed and fabricated for single-mode quasi-TE propagation in the $H = 300$ nm YSZ thin film. (b) YSZ waveguide geometry is characterized by atomic-force microscopy (AFM). Dimensions of the waveguide are $D = 80$ nm for the etching depth and $W = 760$ nm for the width. (c) Simulation of fundamental TE mode under the experimental geometrical values of the YSZ waveguide. (d) X-ray diffraction (XRD) of the YSZ thin film studied on sapphire. The $2\theta - \omega$ XRD scan presents both (002) and (0006) diffraction peaks from YSZ and sapphire substrate, respectively, confirming the only one [001] YSZ growth direction. (e) The ω scan reveals the mosaïcity of the (001) YSZ plans with an FWHM = 0.03°. (f) Propagation losses $\alpha = 3.2$ dB $\cdot$ cm^{-1} are estimated at $\lambda = 1550$ nm thanks to the transmission level of different waveguides, long from 0.8 to 5.8 mm.

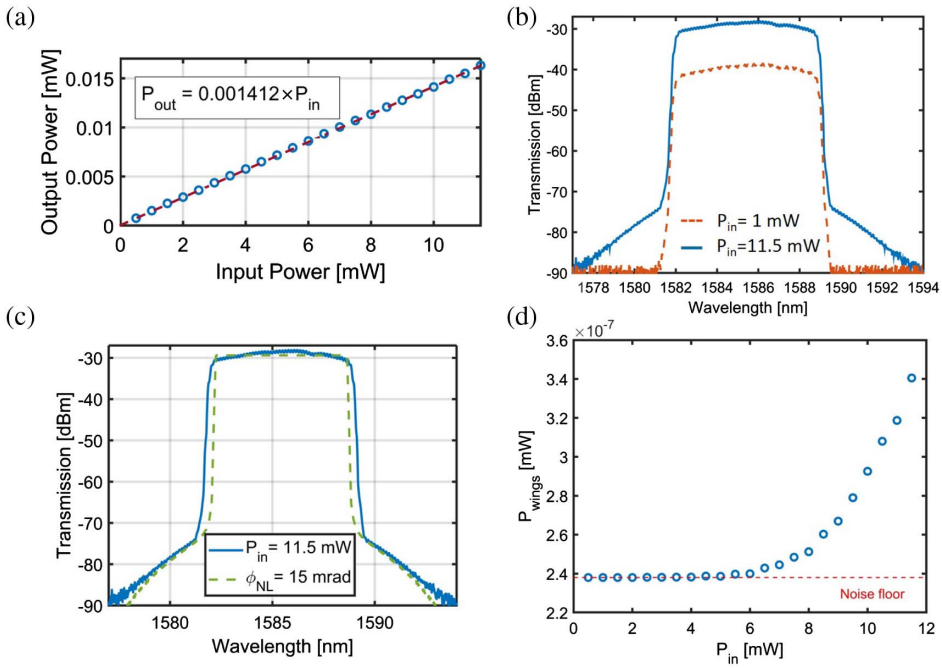

Fig. 5. (a) P_{out} versus P_{in} curve at $\lambda = 1580$ nm revealing the absence of two-photon absorption (TPA), in agreement with the bandgap energy of $E_g > 5$ eV. (b) Optical transmission at low (dashed orange) and high (solid blue) input powers. (c) Simulation (dashed red) of the spectrum transmitting through a YSZ-based waveguide calculated with the experimental parameters. (d) Experimental measurement of the power in the generated frequencies.

adjustable dispersion coefficient $\phi^{(2)}$. In the Fourier limit, the autocorrelation pulse duration has been measured equal to $T_0 = 2$ ps. The polarized beam that exits the stretcher is injected via butt-coupling, using a microscope objective (20×), to the YSZ waveguide, which matches the excitation guided mode in the taper. After the sample, another polarization beam splitter is used to verify the transmitted polarization state.

We first probed, thanks to this setup, the nonlinear absorption of YSZ by measuring the output light power P_{out} for different injected powers P_{in} in the YSZ waveguide. The result, as plotted in Fig. 5(a), shows linear behavior, indicating the absence of two-photon absorption (TPA), as expected due to the YSZ bandgap energy around $E_g = 4.5$ eV [39,40]. From the slope, and considering the two facets of the waveguide equivalent, we also extracted the transmission coefficient of about $\kappa_F = 9.1\%$. The comparison of the output spectra for different input power P_{in} [Fig. 5(b)] reveals a spectral broadening for higher power due to the Kerr effect induced by the constituting material of the waveguide.

In absence of TPA, the nonlinear effective susceptibility of the waveguide can be written as $\mathrm{Re}[\gamma_{wg}] = \phi_{NL}/(\kappa_F P_{in} L_{eff} \eta)$, with ϕ_{NL} the nonlinear phase shift and L_{eff} the effective length given by $L_{eff} = [1 - \exp(-\alpha L)]/\alpha$, where α is the linear propagation losses, and $\eta = 1/[F \int_0^{1/F} |U(t)|^2 dt]$ with $U(t)$ the normalized temporal shape of the pulse.

The mode simulation in Fig. 4(c) reveals the distribution of the electric field intensity propagating through the YSZ waveguide. Being the substrate for the growth of the YSZ thin film, sapphire also interacts with a part of the input power. Then, to extract the nonlinearities of YSZ, both materials have to be considered in the nonlinear response. In a first approach, we can rewrite the waveguide effective nonlinear susceptibility as the contribution of the two nonlinear materials such as

$$\mathrm{Re}[\gamma_{wg}] = \frac{2\pi}{\lambda_0 A_{NL}} (\Gamma_{YSZ} n_2^{YSZ} + \Gamma_{Al_2O_3} n_2^{Al_2O_3}), \quad (4)$$

where $\Gamma_{YSZ} = 36.9\%$ and $\Gamma_{Al_2O_3} = 63.0\%$ are the overlapped power confined in the two materials, λ_0 the wavelength of the pump, A_{NL} the nonlinear area calculated from the mode simulation, and n_2 the nonlinear refractive index. The nonlinear Kerr index from sapphire was taken from Ref. [47] and equals to $n_2^{Al_2O_3} \approx 3 \times 10^{-20}$ m$^2 \cdot$W^{-1}. For the maximum input average power $P_{in} = 11.5$ mW, the corresponding nonlinear phase shift ϕ_{NL} is simulated to be 15 mrad, as represented in Fig. 5(c). This value leads to an effective Kerr nonlinear coefficient in YSZ, which equals to $n_2^{YSZ} \approx 4.0 \pm 2 \times 10^{-19}$ m$^2 \cdot$W^{-1}, being one order of magnitude larger than in sapphire and similar to the silicon nitride [48]. Furthermore, we have performed the analysis of the spectral broadening behavior by plotting in Fig. 5(d) the power contained in the symmetric wings P_{wings} of the measured output spectra for the different input powers. For input power lower than 6 mW, P_{wings} is constant, limited to the noise floor of the optical spectrum analyzer. For higher powers, a quadratic variation of P_{wings} is observed in accordance with the variation of the Kerr-induced spectral broadening, which is expected to be proportional to P_{in}^2 for $\phi_{NL} \ll 1$ [49].

4. DISCUSSION

As YSZ is a crystal, n_2^{YSZ} is a tensor as well as the third-order nonlinear susceptibility $\chi_{YSZ}^{(3)}$. The in-plane orientation of YSZ grains in the waveguide is not well defined as in classical silicon

substrate; further, the electric-field direction of the pump is not aligned along only one crystallographic direction. Thanks to a complete material characterization of our films [22], we considered as a first approximation that the electric field of the pump is aligned equiprobably in the [100] and [110] directions. In this case, the experimental value n_2^{YSZ} becomes an effective value $\hat{n}_2^{YSZ}$, which can be compared with the theory via an effective third-order nonlinear susceptibility $\hat{\chi}^{(3)}_{YSZ}$, defined as follows:

$$\hat{\chi}^{(3)}_{YSZ} = \frac{\chi^{(3)}_{YSZ,\langle 100\rangle} + \chi^{(3)}_{YSZ,\langle 110\rangle}}{2}, \tag{5}$$

where it has been demonstrated that, for a cubic crystal,

$$\chi^{(3)}_{YSZ,\langle 100\rangle} = \chi^{(3)}_{YSZ,xxxx}, \tag{6}$$

and

$$\chi^{(3)}_{YSZ,\langle 110\rangle} = \frac{\chi^{(3)}_{YSZ,xxxx} + 3\chi^{(3)}_{YSZ,xxyy}}{2}.$$

Using the calculated values for YSZ 7%, as presented in Table 3, we found a theoretical effective susceptibility of $\hat{\chi}^{(3)}_{YSZ} = 2.00 \times 10^{-21}\ m^2 \cdot V^{-2}$ at the B3LYP level of theory, leading to the birefringence $\Delta n = \hat{n}_2 I$, where I is the laser radiation power per unit surface, with the in-plane refractive index $\hat{n}_2 = 3\hat{\chi}^{(3)}/4c\varepsilon_0\epsilon = 1.3 \times 10^{-19}\ m^2 \cdot W^{-1}$ (ϵ is the relative dielectric in-plane ϵ_{xx} component, ε_0 represents the electric permittivity of vacuum, and c represents the light velocity).

The theoretical value for YSZ 7% is close to the one of pure c-ZrO_2, which, at the same level of theory, is estimated to lie only 1.2 times higher (e.g., $1.3 \times 10^{-19}\ m^2 \cdot W^{-1}$ for YSZ versus $1.6 \times 10^{-19}\ m^2 \cdot W^{-1}$ for c-ZrO_2 at the B3LYP level of theory).

The convergence between experiment and theory is expected to improve if two additional factors are to be considered. The first concerns the vibrational contributions to the third-order NLO responses of the systems considered. To address these effects, we computed Raman intensities with the CRYSTAL code, which depend on the variation of the dipole polarizability of the unit cell with respect to atomic displacements. The outcomes of this brief investigation at the PBE0 level of theory and the basis set of Table 3 suggest that the total

Table 3. Electronic Contribution to the Dielectric Susceptibilities (ϵ_{xx}), Third-Order Susceptibilities ($\chi^{(3)}_{xxxx,xxyy} \times 10^{-21}\ m^2 \cdot V^{-2}$), Effective Third-Order Susceptibilities ($\hat{\chi}^{(3)} \times 10^{-21}\ m^2 \cdot V^{-2}$), and Nonlinear Refractive Index ($\hat{n}_2 \times 10^{-19}\ m^2 \cdot W^{-1}$) of YSZ 7% in Y_2O_3 [Fig. 3(a)] Computed at the PBE0 and B3LYP Levels of Theory on PBE0 Optimized Local Crystal Structures[a]

	ϵ_{xx}	$\chi^{(3)}_{xxxx}$	$\chi^{(3)}_{xxyy}$	$\hat{\chi}^{(3)}$	$\hat{n}_2$
PBE0	4.24	1.20	0.99	1.64	1.1
B3LYP	4.33	1.48	1.19	2.00	1.3
B3LYP(+spd)	4.75	1.65	1.23	2.16	1.3

[a]For Zr, Y atoms, we used the pseudo-potential (ECP) basis set of Hay and Wadt (Zr[3s1p1d], Y[2s1p1d]), for O atoms the Durand–Barthelat ECP basis ([2s1p]).

IDRI second unit-cell hyperpolarizabilities [50] (γ^{tot}_{IDRI}) of the pure and doped c-ZrO_2, defined as $\gamma^{tot}_{IDRI} = \gamma^{vib}_{IDRI} + \gamma^{e}$, should be about 10% larger than γ^e, regardless of the laser "high-frequency" (~6500 cm^{-1}). The second factor, precisely, should involve frequency dispersion effects on γ^e, which have not been treated here under periodic boundary conditions due to software limitations. Nevertheless, we estimate that, for the experimental laser wavelength, corresponding to a photon energy of 0.8 eV ($\lambda = 1550$ nm), and a solid with a gap around 5 eV, the electronic part of IDRI $\chi^{(3)}(-\omega;\omega,-\omega,\omega)$ should experience a maximum increase of 10%, under the hypothesis that the UV-absorption spectrum has a strong absorption peak precisely at the gap. The respective guesstimate is further supported by time-dependent DFT (TD-DFT) sum-over-state (SOS) computations conducted on two out of the three nanoclusters considered in this work, namely, $(ZrO_2)_4$ and $(ZrO_2)_8$ (for more details, see Appendix A). Furthermore, owing to its positive coefficient of thermal expansion, the cell parameter of ZrO_2 is expected to increase as the temperature rises. This effect, not considered in the calculation, could deliver an additional small increase of $\chi^{(3)}$. Similarly, the strain induced in the YSZ thin film by the sapphire substrate during the growth could also be considered as an additional source of the observed deviation between theory and experiment.

5. CONCLUSION

In conclusion, we present in this work a detailed theoretical and experimental study of the third-order nonlinearities of YSZ. The IDRI Kerr property has been first predicted with *ab-initio* calculations for different unit cell configurations and compositions. As the nonlinearities increase when the yttrium-doping concentration decreases, we have experimentally fabricated and characterized YSZ waveguides with a minimum of 8% of Y_2O_3, thus ensuring the cubic structure. The nonlinearity birefringence $n_2^{YSZ} \approx 4.0 \pm 2 \times 10^{-19}\ m^2 \cdot W^{-1}$ experimentally measured is compared with the predicted static theoretical value, $\hat{n}_2 \approx 1.3 \times 10^{-19}\ m^2 \cdot W^{-1}$, which is expected to rise up to $\hat{n}_2 \approx 1.6 \times 10^{-19}\ m^2 \cdot W^{-1}$ if vibrational and dispersion effects are to be taken into account.

The obvious convergence between experiment and theory demonstrates the robustness of our method to characterize the nonlinearities of new materials. Furthermore, the computational results exposed that, for low concentrations in Y_2O_3, YSZ IDRI Kerr should lie close to that of pure c-ZrO_2, which is not stable in ambient conditions. The latter outcome originates from the inverse proportionality of both ϵ and $\chi^{(3)}$ to the amount of Y_2O_3 units comprised in the local atomistic structure of YSZ ($n_2 \propto \chi^{(3)}/\epsilon$). Hence, although Y doping weakens the third-order nonlinearities of pure c-ZrO_2, it does not have a dramatic impact on its Kerr index (IDRI), which is of critical importance in photonic applications. Therefore, the current theoretical and experimental investigation highlights the potential of YSZ to be used as a new material for nonlinear optics.

APPENDIX A

Sample Fabrication

Sapphire (0001) substrates are cleaned with ethanol and annealed at 1200°C in air for 4 h before deposition. Laser ablation

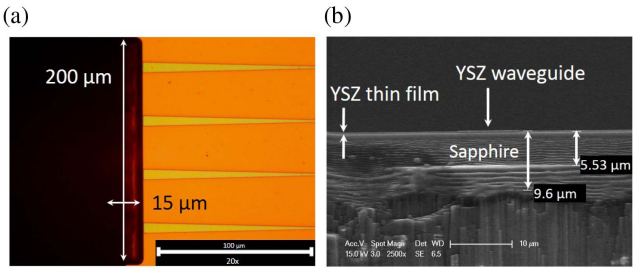

Fig. 6. Waveguides facets obtained with the two-step dicing procedure, including classical dicing technique and focus ion-beam (FIB) etching. (a) Top view of the sample edges with optical microscopy and (b) cross-section observation of a waveguide facet by SEM. Whereas the first classical technique allows to mechanically dice the whole sample, the FIB technique etches a small area, here the extremities of the waveguides, leaving highly transmissive facets.

of 8% yttria-stabilized zirconia rotating ceramic target is carried out in a high vacuum stainless-steel chamber with a base pressure of 10^{-6} Torr. The KrF excimer pulsed laser ($\lambda = 248$ nm, 3 J · cm^{-2}, 5 Hz repetition rate) irradiates the target with an incidence angle of 45°. The deposition occurs in a controlled oxygen atmosphere of 30 mTorr with the substrate placed at 50 mm from the target and heated to 800°C. YSZ thin films on sapphire are then cooled down to room temperature under 300 Torr of oxygen at 10°C · min^{-1} after deposition. Film thickness is measured with spectroscopic ellipsometry (J.A. Woollam). Structural properties and crystallinity of the film are investigated with high-resolution X-ray diffraction (XRD) using a PANalytical X'Pert Pro diffractometer and transmission electron microscopy (TEM) using an aberration probe-corrected FEI Titan Themis microscope. Roughness of the film and geometry parameters (etching depth, width, etc.) of the rib waveguides are characterized with atomic force microscopy (AFM). YSZ rib waveguides are fabricated by electron-beam lithography in a 200 nm thick hydrogen silsesquioxane (HSQ) electron resist layer. The charging effect during the writing, due to the insulator behavior of YSZ and sapphire, is avoided by covering the resist with a 20 nm thick gold layer. The etching is performed with an optimized ion beam etching (IBE) technique using argon ions, accelerated with a voltage of 250 V and sputtering the sample with an incidence angle of 20° from the normal. Butt-coupling injection, required for third-order nonlinear optical characterization, is achieved by opening each facet of the YSZ waveguides by a two-step dicing procedure, which includes first a mechanical dicing technique and second a focused ion beam (FIB) etching technique, using an FEI Scios dual beam. Pictures of the open facets are presented in Fig. 6.

Computational Details

The truncation criteria of the Coulomb and exchange infinite lattice series in the self-consistent field (SCF) calculation are controlled by five thresholds, T_i, which have been set to 8 (T_1–T_4) and 16 (T_5). The number of k-points in the irreducible Brillouin zone (IBZ) of the reciprocal space has been fixed by the shrinking factors equal to 8 (35 k-points in the IBZ for the symmetric c-ZrO_2 structure). The default numerical integration grid (XLGRID) has been used for DFT, and convergence thresholds on self-consistent-field (SCF) energy have been set to 10^{-7} Hartree for structural optimizations (see crystal's manual for more details on the parameters [51]). Calculation of the electronic contribution to polarizability (α^e) and hyperpolarizabilities (β^e and γ^e) of a unit cell is done with the coupled-perturbed Hartree–Fock and Kohn–Sham (CPHF/KS) method [52] implemented in the CRYSTAL code for both finite molecular and infinite periodic systems [53–56]. For Zr and Y atoms, we relied on pseudo-potential (ECP) basis set substrates constructed by Hay and Wadt. In this set, the 12 and 11 valence electrons of Zr and Y, respectively, are described by the (5sp,4d)/[3sp,2d] and (4sp,2d)/[2sp1d] sets of Gaussian-type functions, while the remaining 28 core electrons are approximated by a nonrelativistic potential. For O atoms, the Durand–Barthelat ECP basis set substrate was chosen in which the $1s^2$ core electrons are approximated by a nonrelativistic potential, and the valence electrons are described by a (4sp)/[2s1p] all electron set. The respective basis sets have been successfully used by Ricca *et al.* [34] in the study of YSZ surfaces.

Table 4. Electronic Contribution to the Second-Order Dipole Hyperpolarizability Axial Tensorial Components of $Zr_4O_8Zr_4O_8$, Zr_4O_8 Computed at the HF, MP2 CCSD(T) B3LYP, PBE0, and PBE Levels of Theory with the Def2-SVPD Basis Set (Zr:ECP(28 Core Electrons)(7s7p5d1f)/[5s4p2d1f](valence), O:(8s5p2d)/[4s3p2d])[a]

Method	γ_{xxxx}	γ_{yyyy}	γ_{zzzz}
Zr_4O_8			
HF	16.0	19.6	13.4
MP2	32.4	37.7	26.8
CCSD(T)	37.6	42.0	27.5
B3LYP	39.4	47.1	28.8
PBE0	34.3	40.7	25.6
PBE	57.4	67.1	38.9
Zr_8O_{16}			
HF	35.7	25.1	20.5
MP2	87.7	56.2	40.5
B3LYP	104.7	61.1	39.4
PBE0	90.4	53.2	36.1
PBE	166.9	85.3	51.7
$Zr_{15}O_{30}$			
HF	49.5	34.3	50.7
MP2	106.4	69.3	106.7
B3LYP	104.3	73.1	127.8
PBE0	94.1	62.7	112.7
PBE	193.1	99.2	208.2

[a]All values have been divided by 10^3; they are given in atomic units.

Third-Order Nonlinearities of c-ZrO_2

As seen in Table 1 of the main article, all methods considered provide cell parameters close to the experiment. In the case of the computed bandgaps, PBE0 and B3LYP hybrid functionals overestimate by 0.8 (0.9) and 0.3 (0.4) eV, respectively, the experimentally determined values reported by McComb [40] and Elizalde *et al.* [39]. The latter DFT methods also provide (optical) dielectric constants, which are found in good

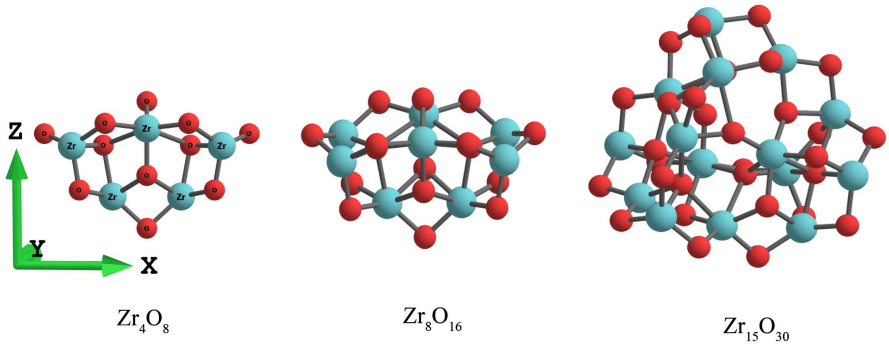

Fig. 7. Most stable structures of $Zr_4O_8Zr_8O_{16}$ and $Zr_{15}O_{30}$.

agreement with available experimental data. On the other hand, the PBE pure functional delivered a bandgap value that lies about 1.5 eV lower than the experimentally determined one and overestimates the experimental dielectric constant. To obtain a rough estimation of the influence of the dynamic electron correlation on the computed bulk nonlinearities, we performed computations using the Hartree–Fock (HF) approximation, which does not treat dynamic electron correlation effects. The computed HF large bandgap of 13.2 eV and the considerably weaker HF $\chi^{(3)}_{iiii}$ and $\chi^{(3)}_{iijj}$ values of 0.13×10^{-21} and 0.19×10^{-21} m^2/V^2, respectively, demonstrate that electron correlation effects, by definition taken into account in DFT, should be of decisive importance for the accurate theoretical determination of the nonlinearities of pure c-ZrO_2. To check the influence of the basis set applied, we added to the initial basis set, one diffuse sp-Gaussian-type function for Zr and one d-type polarization function on each O atom of c-ZrO_2. The obtained values of 2.0×10^{-21} m^2/V^2 for $\chi^{(3)}_{iiii}$ and 1.5×10^{-21} m^2/V^2 for $\chi^{(3)}_{iijj}$, at the B3LYP level, reveal that, if a richer basis set is chosen, no dramatic changes on the computed bulk optical nonlinearities should be expected. Here, it is important to note that the obvious choice to add a set of diffuse sp functions on O atoms has proven impractical due to severe convergence problems in the SCF procedure. Finally, the replacement of ECP basis set for O by an all-electron basis (8s6sp2d)/[1s3sp2d]) [57]) did not bring important changes to the computed third-order optical nonlinearities. For instance, at the PBE0 level, the latter basis set yielded a value of 1.65×10^{-21} m^2/V^2 for $\chi^{(3)}_{iiii}$, while for $\chi^{(3)}_{iijj}$ a value of 1.25×10^{-21} m^2/V^2 was obtained.

Concerning the computed optical nonlinearities (electronic contribution), the largest responses are delivered by the pure PBE functional, which overshoots both $\chi^{(3)}_{iiii}$ and $\chi^{(3)}_{iijj}$ values by a factor of 5 and 2, respectively, as compared with the PBE0 and B3LYP functionals. The observed method dependence is in accord with the results listed in Table 4, which summarizes the second dipole hyperpolarizability axial tensorial components of $Zr_4O_8Zr_8O_{16}$ and $Zr_{15}O_{30}$ (Fig. 7) computed at the HF, MP2 CCSD(T) B3LYP, PBE0, and PBE levels with a sufficiently flexible basis set that is expected to provide a reliable description of dynamic electron correlation effects at the MP2 and CCSD(T) levels of theory. Out of the three functionals considered here, B3LYP and PBE0 delivered values close to those obtained at CCSD(T) and MP2 levels. On the other hand, the pure PBE functional yielded largely overestimated microscopic second hyperpolarizabilities for either cluster size. Finally, to verify our qualitative estimation about the frequency dispersion effects reported in the main text, we studied the dynamic microscopic hyperpolarizabilities of Zr_4O_8 and Zr_8O_{16} clusters at the time-dependent PBE0 level of theory (TD-PBE0) using the widely applied sum-over-state (SOS) treatment developed by Orr and Ward [42,58]. At this level of theory, which showed good performance in the calculation of cluster static hyperpolarizabilities, the computed optical gaps of Zr_4O_8 and Zr_8O_{16} (4.6 and 5.3 eV, respectively) are comparable with the vertical bandgap of the bulk. The outcomes of our SOS computations obtained with the Jorge-DZP all-electron [59] basis set over the first 100 singlet excited states showed that the IDRI dynamic average second hyperpolarizability $\bar{\gamma}(-\omega;\omega,-\omega,\omega)$ ($\omega = 1550$ nm) should lie 11% and 10% higher than the static values of Zr_4O_8 and Zr_8O_{16}, respectively.

Funding. European Research Council (647342); Agence Nationale de la Recherche (10-EQPX-0050).

Acknowledgment. This project received funding from the ERC under the European Union's Horizon 2020 research and innovation program (ERC POPSTAR), the French Industry Ministry Nano 2017 program, and the ANR FOIST. The authors also acknowledge C2N Nanocenter of the French RENATECH network, where the devices were fabricated, ANR "Investissement d'Avenir" program for having funded the acquisition of the NANOTEM platform, including a dual-beam FIB-FEG FEI SCIOS system used in this work. Part of this work was granted access to the HPC resources of [CCRT/CINES/IDRIS] under the allocation 2018–2019 and 2019–2020 [A0040807031] made by GENCI (Grand Equipement National de Calcul Intensif). We also acknowledge the "Direction du Numérique" of the Université de Pau et des Pays de l'Adour for the computing facilities provided.

Disclosures. The authors declare no conflict of interest.

[†]These authors contributed equally to this work.

REFERENCES

1. H. Rong, R. Jones, A. Liu, O. Cohen, D. Hak, A. Fang, and M. Paniccia, "A continuous-wave Raman silicon laser," Nature **433**, 725–728 (2005).
2. E. A. Kittlaus, H. Shin, and P. T. Rakich, "Large Brillouin amplification in silicon," Nat. Photonics **10**, 463–467 (2016).
3. M. A. Foster, A. C. Turner, J. E. Sharping, B. S. Schmidt, M. Lipson, and A. L. Gaeta, "Broad-band optical parametric gain on a silicon photonic chip," Nature **441**, 960–963 (2006).
4. D. J. Moss, R. Morandotti, A. L. Gaeta, and M. Lipson, "New CMOS-compatible platforms based on silicon nitride and hydex for nonlinear optics," Nat. Photonics **7**, 597–603 (2013).
5. K. Narayanan and S. F. Preble, "Optical nonlinearities in hydrogenated-amorphous silicon waveguides," Opt. Express **18**, 8998–9005 (2010).
6. S. Dai, F. Chen, Y. Xu, Z. Xu, X. Shen, T. Xu, R. Wang, and W. Ji, "Mid-infrared optical nonlinearities of chalcogenide glasses in Ge-Sb-Se ternary system," Opt. Express **23**, 1300–1307 (2015).
7. C. Thu, P. Ehrenreich, K. K. Wong, E. Zimmermann, J. Dorman, W. Wang, A. Fakharuddin, M. Putnik, C. Drivas, A. Koutsoubelitis, M. Vasilopoulou, L. C. Palilis, S. Kennou, J. Kalb, T. Pfadler, and L. Schmidt-Mende, "Role of the metal-oxide work function on photocurrent generation in hybrid solar cells," Sci. Rep. **8**, 3559 (2018).
8. C. López-Gándara, F. M. Ramos, and A. Cirera, "YSZ-based oxygen sensors and the use of nanomaterials: a review from classical models to current trends," J. Sens. **2009**, 258489 (2009).
9. R. Ramesh and D. G. Schlom, "Whither oxide electronics?" MRS Bull. **33**, 1006–1014 (2008).
10. M. Bazzan and C. Sada, "Optical waveguides in lithium niobate: recent developments and applications," Appl. Phys. Rev. **2**, 040603 (2015).
11. L. Mechin, "YBCO superconducting microbolometers fabricated by silicon micromachining," Ph.D. thesis (Université de Caen, 1996).
12. X. D. Wu, R. E. Muenchausen, N. S. Nogar, A. Pique, R. Edwards, B. Wilkens, T. S. Ravi, D. M. Hwang, and C. Y. Chen, "Epitaxial yttria-stabilized zirconia on (1102) sapphire for $YBa_2Cu_3O_{7-\delta}$thin films," Appl. Phys. Lett. **58**, 304–306 (1991).
13. L. F. Chen, P. F. Chen, L. Li, S. L. Li, X. N. Jing, S. J. Pan, and Y. H. Guo, "$YBa_2Cu_3O_7$ thin films grown on sapphire with epitaxial yttria-stabilized zirconia buffer layers," Appl. Phys. Lett. **61**, 2412–2413 (1992).
14. C. Jorel, H. Colder, A. Galdi, and L. Méchin, "Epitaxial PZT thin films on YSZ-buffered Si (001) substrates for piezoelectric MEMS or NEMS applications," IOP Conf. Ser.: Mater. Sci. Eng. **41**, 012012 (2012).
15. T. Falcade and C. de Fraga Malfatti, "Fuel cell: a review and a new approach about YSZ solid oxide electrolyte deposition direct on LSM porous substrate by spray pyrolysis," in *Electrochemical Cells-New Advances in Fundamental Researches and Applications* (InTech, 2012), pp. 139–160.
16. S. Heiroth, R. Ghisleni, T. Lippert, J. Michler, and A. Wokaun, "Optical and mechanical properties of amorphous and crystalline yttria-stabilized zirconia thin films prepared by pulsed laser deposition," Acta Materialia **59**, 2330–2340 (2011).
17. X. Song, Z. Liu, M. Kong, C. Lin, L. Huang, X. Zheng, and Y. Zeng, "Thermal stability of yttria-stabilized zirconia (YSZ) and YSZ Al_2O_3 coatings," Ceram. Int. **43**, 14321–14325 (2017).
18. M. F. Manna, D. E. Grandstaff, G. C. Ulmer, and E. P. Vicenzi, "The chemical durability of yttria-stabilized ZrO_2 pH and O_2 geothermal sensors," in *Proceedings of the Tenth International Symposium on Water Rock Interaction* (2001), pp. 295–299.
19. S. K. Pandey, O. P. Thakur, R. Raman, A. Goyal, and A. Gupta, "Structural and optical properties of YSZ thin films grown by PLD technique," Appl. Surf. Sci. **257**, 6833–6836 (2011).
20. R. C. Buchanan and S. Pope, "Optical and electrical properties of yttria stabilized zirconia (YSZ) crystals," J. Electrochem. Soc. **130**, 962–966 (1983).
21. N. Nicoloso, A. Löbert, and B. Leibold, "Optical absorption studies of tetragonal and cubic thin-film yttria-stabilized zirconia," Sens. Actuators B Chem. **8**, 253–256 (1992).
22. G. Marcaud, S. Matzen, C. Alonso-Ramos, X. Le Roux, M. Berciano, T. Maroutian, G. Agnus, P. Aubert, L. Largeau, V. Pillard, S. Serna, D. Benedikovic, C. Pendenque, E. Cassan, D. Marris-Morini, P. Lecoeur, and L. Vivien, "High-quality crystalline yttria-stabilized-zirconia thin layer for photonic applications," Phys. Rev. Mater. **2**, 035202 (2018).
23. K. K. Gopalan, D. Rodrigo, B. Paulillo, K. K. Soni, and V. Pruneri, "Ultrathin yttria-stabilized zirconia as a flexible and stable substrate for infrared nano-optics," Adv. Opt. Mater. **7**, 1800966 (2019).
24. S. Serna and N. Dubreuil, "Bi-directional top-hat D-Scan: single beam accurate characterization of nonlinear waveguides," Opt. Lett. **42**, 3072–3075 (2017).
25. M. A. Parkes, K. Refson, M. D'Avezac, G. J. Offer, N. P. Brandon, and N. M. Harrison, "Chemical descriptors of yttria-stabilized zirconia at low defect concentration: an *ab initio* study," J. Phys. Chem. A **119**, 6412–6420 (2015).
26. M. A. Parkes, D. A. Tompsett, M. D'Avezac, G. J. Offer, N. P. Brandon, and N. M. Harrison, "The atomistic structure of yttria stabilised zirconia at 6.7 mol%: an *ab initio* study," Phys. Chem. Chem. Phys. **18**, 31277–31285 (2016).
27. D. M. Bishop, "Molecular vibrational and rotational motion in static and dynamic electric fields," Rev. Mod. Phys. **62**, 343–374 (1990).
28. P. Karamanis, R. Marchal, P. Carbonnière, and C. Pouchan, "Doping-enhanced hyperpolarizabilities of silicon clusters: a global *ab initio* and density functional theory study of $Si_{10}(Li, Na, K)_n$ (n = 1, 2) clusters," J. Chem. Phys. **135**, 044511 (2011).
29. P. Karamanis, C. Pouchan, C. A. Weatherford, and G. L. Gutsev, "Evolution of properties in prolate $(GaAs)_n$ clusters," J. Phys. Chem. C **115**, 97–107 (2011).
30. P. Karamanis, "The importance of the DFT method on the computation of the second hyper polarizability of semiconductor clusters of increasing size: a critical analysis on prolate aluminum phosphide clusters," Int. J. Quantum Chem. **112**, 2115–2125 (2012).
31. J. P. Perdew, K. Burke, and M. Ernzerhof, "Generalized gradient approximation made simple," Phys. Rev. Lett. **77**, 3865–3868 (1996).
32. C. Adamo and V. Barone, "Toward reliable density functional methods without adjustable parameters: the PBE0 model," J. Chem. Phys. **110**, 6158–6170 (1999).
33. A. D. Becke, "Density-functional thermochemistry. III. The role of exact exchange," J. Chem. Phys. **98**, 5648–5652 (1993).
34. C. Ricca, A. Ringuedé, M. Cassir, C. Adamo, and F. Labat, "Revealing the properties of the cubic ZrO_2 (111) surface by periodic DFT calculations: reducibility and stabilization through doping with aliovalent Y_2O_3," RSC Adv. **5**, 13941–13951 (2015).
35. R. Dovesi, A. Erba, R. Orlando, C. M. Zicovich-Wilson, B. Civalleri, L. Maschio, M. Ferrabone, M. Rérat, S. Casassa, J. Baima, S. Salustro, and B. Kirtman, "Quantum-mechanical condensed matter simulations with crystal," WIREs Comput. Mol. Sci. **8**, e1360 (2018).
36. M. J. Frisch, G. W. Trucks, H. B. Schlegel, G. E. Scuseria, M. A. Robb, J. R. Cheeseman, G. Scalmani, V. Barone, B. Mennucci, G. A. Petersson, H. Nakatsuji, M. Caricato, X. Li, H. P. Hratchian, A. F. Izmaylov, J. Bloino, G. Zheng, J. L. Sonnenberg, M. Hada, M. Ehara, K. Toyota, R. Fukuda, J. Hasegawa, M. Ishida, T. Nakajima, Y. Honda, O. Kitao, H. Nakai, T. Vreven, J. A. Montgomery, Jr., J. E. Peralta, F. Ogliaro, M. Bearpark, J. J. Heyd, E. Brothers, K. N. Kudin, V. N. Staroverov, R. Kobayashi, J. Normand, K. Raghavachari, A. Rendell, J. C. Burant, S. S. Iyengar, J. Tomasi, M. Cossi, N. Rega, J. M. Millam, M. Klene, J. E. Knox, J. B. Cross, V. Bakken, C. Adamo, J. Jaramillo, R. Gomperts, R. E. Stratmann, O. Yazyev, A. J. Austin, R. Cammi, C. Pomelli, J. W. Ochterski, R. L. Martin, K. Morokuma, V. G. Zakrzewski, G. A. Voth, P. Salvador, J. J. Dannenberg, S. Dapprich, A. D. Daniels, O. Farkas, J. B. Foresman, J. V. Ortiz, J. Cioslowski, and D. J. Fox, *Gaussian09 Revision D.01* (Gaussian Inc., 2009).
37. E. V. Stefanovich, A. L. Shluger, and C. R. A. Catlow, "Theoretical study of the stabilization of cubic-phase ZrO_2 by impurities," Phys. Rev. B **49**, 11560–11571 (1994).
38. R. A. Ploc, "The lattice parameter of cubic ZrO_2 formed on zirconium," J. Nucl. Mat. **99**, 124–128 (1981).
39. E. Elizalde, J. M. Sanz, F. Yubero, and L. Galan, "Determination of optical constants of ZrO_2 and Zr by electron energy-loss spectroscopy," Surf. Interface Anal. **16**, 213–214 (1990).

40. D. W. McComb, "Bonding and electronic structure in zirconia pseudopolymorphs investigated by electron energy-loss spectroscopy," Phys. Rev. B **54**, 7094–7102 (1996).
41. D. L. Wood and K. Nassau, "Refractive index of cubic zirconia stabilized with yttria," Appl. Opt. **21**, 2978–2981 (1982).
42. B. Orr and J. Ward, "Perturbation theory of the non-linear optical polarization of an isolated system," Mol. Phys. **20**, 513–526 (1971).
43. S. J. A. van Gisbergen, P. R. T. Schipper, O. V. Gritsenko, E. J. Baerends, J. G. Snijders, B. Champagne, and B. Kirtman, "Electric field dependence of the exchange-correlation potential in molecular chains," Phys. Rev. Lett. **83**, 694–697 (1999).
44. L. Zibordi-Besse, Y. Seminovski, I. Rosalino, D. Guedes-Sobrinho, and J. L. F. Da Silva, "Physical and chemical properties of unsupported $(MO_2)_n$ clusters for M = Ti, Zr, or Ce and n = 1–15: a density functional theory study combined with the tree-growth scheme and Euclidean similarity distance algorithm," J. Phys. Chem. C **122**, 27702–27712 (2018).
45. J. Zaanen, G. A. Sawatzky, and J. W. Allen, "Bandgaps and electronic structure of transition-metal compounds," Phys. Rev. Lett. **55**, 418–421 (1985).
46. S. Serna, J. Oden, M. Hanna, C. Caer, X. L. Roux, C. Sauvan, P. Delaye, E. Cassan, and N. Dubreuil, "Enhanced nonlinear interaction in a microcavity under coherent excitation," Opt. Express **23**, 29964–29977 (2015).
47. A. Major, F. Yoshino, I. Nikolakakos, J. S. Aitchison, and P. W. Smith, "Dispersion of the nonlinear refractive index in sapphire," Opt. Lett. **29**, 602–604 (2004).
48. K. Ikeda, R. E. Saperstein, N. Alic, and Y. Fainman, "Thermal and Kerr nonlinear properties of plasma-deposited silicon nitride/silicon dioxide waveguides," Opt. Express **16**, 12987–12994 (2008).
49. S. C. Pinault and M. Potasek, "Frequency broadening by self-phase modulation in optical fibers," J. Opt. Soc. Am. B **2**, 1318–1319 (1985).
50. B. Champagne, E. A. Perpète, J.-M. André, and B. Kirtman, "Analysis of the vibrational static and dynamic second hyperpolarizabilities of polyacetylene chains," Synth. Met. **85**, 1047–1050 (1997).
51. R. Dovesi, V. R. Saunders, C. Roetti, R. Orlando, C. M. Zicovich-Wilson, F. Pascale, B. Civalleri, K. Doll, N. M. Harrison, I. J. Bush, P. D'Arco, M. Llunell, M. Causà, Y. Noël, L. Maschio, A. Erba, M. Rérat, and S. Casassa, *CRYSTAL17 User's Manual* (University of Torino, 2017).
52. G. Hurst, M. Dupuis, and E. Clementi, "Ab initio analytic polarizability, first and second hyperpolarizabilities of large conjugated organic molecules: applications to polyenes C_4H_6 to $C_{22}H_{24}$," J. Chem. Phys. **89**, 385–395 (1988).
53. M. Ferrero, M. Rérat, R. Orlando, and R. Dovesi, "The calculation of static polarizabilities of periodic compounds. The implementation in the CRYSTAL code for 1D, 2D and 3D systems," J. Comp. Chem. **29**, 1450–1459 (2008).
54. M. Ferrero, M. Rérat, R. Orlando, and R. Dovesi, "Coupled perturbed Hartree-Fock for periodic systems: the role of symmetry and related computational aspects," J. Chem. Phys. **128**, 014110 (2008).
55. R. Orlando, V. Lacivita, R. Bast, and K. Ruud, "Calculation of the first static hyperpolarizability tensor of three-dimensional periodic compounds with a local basis set: a comparison of LDA, PBE, PBE0, B3LYP, and HF results," J. Chem. Phys. **132**, 244106 (2010).
56. M. Ferrero, M. Rérat, B. Kirtman, and R. Dovesi, "Calculation of first and second static hyperpolarizabilities of one- to three-dimensional periodic compounds. Implementation in the CRYSTAL code," J. Chem. Phys. **129**, 244110 (2008).
57. L. Valenzano, F. J. Torres, K. Doll, F. Pascale, C. M. Zicovich-Wilson, and R. Dovesi, "*Ab initio* study of the vibrational spectrum and related properties of crystalline compounds; the case of $CaCO_3$ calcite," Zeitschrift für Physikalische Chemie **220**, 893–912 (2006).
58. T. Lu and F. Chen, "Multiwfn: a multifunctional wavefunction analyzer," J. Comput. Chem. **33**, 580–592 (2018).
59. K. L. Schuchardt, B. T. Didier, T. Elsethagen, L. Sun, V. Gurumoorthi, J. Chase, J. Li, and T. L. Windus, "Basis set exchange: a community database for computational sciences," J. Chem. Inf. Model. **47**, 1045–1052 (2007).